SciencePG
Science Publishing Group

Research Article

Prospecting Tungsten (Scheelite) Mineralization in the Djouzami Area (Adamawa Cameroon) Using Ultra-Violet (UV) Fluorescence and Landsat-8 OLI Images

Yingyang Wanbitching Raoul[1, *] ⓘ, Nomo Negue Emmanuel[2 *] ⓘ,
Nguihdama Dagwai[3] ⓘ, Ayiwouo Ngounouno Mouhamed[4] ⓘ,
Mbowou Gbambie Isaac Bertrand[4] ⓘ, Ngounouno Ismaïla[1] ⓘ

[1]Department of Earth Sciences, Faculty of Science, University of Ngaoundere, Ngaoundere, Cameroon

[2]Department of Earth Sciences, Faculty of Science, University of Yaounde I, Yaounde, Cameroon

[3]Department of Earth Sciences, School of Higher Education, University of Maroua, Maroua, Cameroon

[4]School of Geology and Mining Engineering, University of Ngaoundere, Meiganga, Cameroon

Abstract

Remote sensing technology and X-rays fluorescence are largely used in the applied geology field. In this study, we combine field observations and petrography, remote sensing applications through the processing of the Landsat-8 OLI, and Ultra-violet fluorescence to map geological structures, hydrothermal alteration minerals, and characterize tungsten mineralization in the Djouzami area (Adamawa, Cameroon). Landsat-8 OLI satellite imagery, was processed to detect both hydrothermal alteration zones and regional structural lineaments associated with tungsten mineralization. Fieldworks and petrography revealed hydrothermal mineral assemblage made of muscovite, chlorite, tourmaline, hematite, calcite and sericite associated to metallic minerals including tungsten and pyrite hosted in quartz veins. This hydrothermal mineral assemblage is also identified in the gold-bearing quartz veins reported in several areas along the Lom group. Band Ratio (BR) and Principal component analysis (PCA) were implemented to extract spectral information related to alteration minerals. The Band Ratios 6/7, 4/2, and 6/5 have permits to map clay, iron oxide/hydroxides, and ferrous minerals, respectively. This study demonstrates the significant potential of fieldwork and multispectral remote sensing data processing for tungsten prospecting as a mineral exploration technique in the Djouzami region. The mapping led to the detection of 1334 lineaments which show four main directions. The ENE-WSW directions corresponds to the trending of the Sanaga shear zone; the NE-SW direction represents the trending of the Djouzami and the Bétaré-Oya shear zones or the main shear zone which underline the Lom group; the N-S and E-W directions are equivalent to the trending of the foliation in the Meiganga area. Most of the high hydrothermal zones and tungsten-bearing quartz veins are located along the NE-SW lineaments or shear zone. Gold-related NE-SW trending Djouzami shear zone is also proposed. The NE-SW structure constitute certainly pathway for mineralizing fluids and ground water circulation, and control tungsten mineralization. Results proposed in this work provide important information for research of characteristic hydrothermal minerals assemblage that accompany tungsten mineralization, and for identify structures that control this mineralization in the area.

*Corresponding author: yingyangraoul@gmail.com (Yingyang Wanbitching Raoul)

1. Introduction

Tungsten is a rare metals or strategic metals, scarce in the nature (1.25 ppm in the terrestrial crust). It is mainly present in the form of wolframite (FeMnWO4), but also as scheelite. (CaWO4). Several types of tungsten deposits are distinguished among which skarns, breccia pipes, rare-metal granites, disseminated greisen-type deposits and vein-type deposits [1, 2]. Tungsten mineralization can be of magmatic and/or hydrothermal origin [3]. Hydrothermal deposits are frequently associated with primary gold mineralization and have a hydrothermal paragenesis consisting of carbonates, epidote, tourmaline and muscovite [4]. Scheelite ore, composed of calcium and tungsten, under UV lighting (254 nanometers). When ores and crystals are exposed to different light sources (white light, infrared, ultraviolet, laser, etc.), the matter of which they are composed interacts with the light. A residual coloration, or luminescence, is then observed. These phenomena make it possible to gather information about the structure of mineral materials, their composition, and their physico-chemical properties without damaging them. Physical color phenomena result from the diffraction of light on materials, while photoluminescence phenomena result from the emission of light by these materials. Scheelite can be recognized petrographically under a short-wave UV lamp, fluorescing pale blue [5-7].

Mineral exploration includes a succession of stages that make it possible to focus on one or more mining targets, starting from one or more favorable mineral occurrences to move towards concentrations high enough and technically exploitable to allow the opening of a mine [8]. Several methods are used for the mineral exploration including remote sensing, coupled with geology, geophysics, geochemistry and reserve estimation methods. Remote sensing has been largely used these last years for mapping lithological units and geological structures, identify hydrothermal alteration zones; and mineral exploration [9-21]. The principle consists to use the spectral signatures of minerals and mineral assemblages formed by hydrothermal alteration to identify outflows of hydrothermal systems, which can support the recognition of mineralized zones [20, 22-26]. Remote sensing technique in mainly employed because it provide a cost-effective approach resulting from his ability to access difficult terrains and landforms (such as some mountains and forest terrains), and data collection can be done rapidly at frequent intervals on a large scale. Hydrothermally altered rocks are frequently indicated by iron oxide, clay, carbonate, and sulfate minerals, which produce diagnostic absorption signatures throughout the visible and near infrared

(VNIR) and shortwave infrared (SWIR) regions [27]. Therefore, image processing methods transform multispectral satellite data into images that enhance geological features in contrast to the background [25, 20, 28-34].

The eastern part of Cameroon in endowed with rare-metal mineralization occurrences, including tungsten [35, 36] but, few studies have been made for the characterization and mapping of this mineralization using remote sensing. During field works in the Djouzami area located along the Lom group, tungsten mineralization associated to quartz veins have been identified. This group is well known for its significant mining potential and in importance of gold mining exploration [20, 37-39].

The goal of this study is to characterize tungsten mineralization and associated hydrothermal minerals assemblage, and define the structure which control this mineralization. This will be done through Ultra-violet (UV) fluorescence analysis of mineralized samples, and Landsat-8 OLI images by study multispectral imagery. The results may provide a tool for mineral exploration in Adamawa Cameroon.

2. Geological Setting and Mineralization

The Djouzami area is located along the Lom group and belongs to the Adamawa-Yadé domain of the Central African Orogenic Belt (Figure 1A) in Cameroon. The Adamawa-Yadé or Central Cameroon domain (Figure 1B) extends from the north of Bafia group, to the Tchollié-Banyo shear zone (TBSZ) [40]. This domain is made of (a) Archaean to Palaeoproterozoic metamorphic rocks (amphibolite, paragneiss, orthogneiss and migmatite) [41-44]. Recently, U-Pb ages on detrital zircon in paragneisses point out the contribution of Archaean, Palaeoproterozoic, and Neoproterozoic sources and suggest a maximum deposition age of 725 ± 12 Ma [45]. Metamorphic rocks of this domain were transformed under high-grade metamorphic conditions (1.3 GPa–770℃) dated between 600 and 582 Ma (U-Pb on zircon data [45-47].; (b) Neoproterozoic metavolcano-sedimentary rocks belonging to the Lom group, recrystallized under low- to medium grade metamorphic conditions during the Panafrican orogeny [46-48]. In addition, some Mbé–Sassa-Berci amphibolite having preserved magmatic zircon grains yielding Neoproterozoic ages of 600 ± 4 and 599 ± 6 Ma (U/Pb on zircon; [45]); (c) syn- to late-orogenic weakly deformed granites emplaced between 600 and 575 Ma [45, 49], showing calc-alkaline to shoshonitic affinity, and considered to be of

crustal melt or having mixed origin [50, 51, 43, 46, 49]. These granitoids displays in place enclaves or xenolith of host rocks (gneiss, migmatite, amphibolite, schists) and are crosscut by aplite, microgranite, pegmatite and quartz veins [52-56]. The abundance of inherited zircon and monazite grains with Archaean to Palaeoproterozoic U-Pb ages in the metasediments and granites of the Adamawa-yadé domain suggests that it is mostly composed of rocks issued from an Archaean to Palaeoproterozoic crust reworked during the Panafrican orogeny [40, 41]; According to [57, 58], the Central Cameroon domain represents an Achaean/Palaeoproterozoic crust, detached from the Congo craton during the early Neoproterozoic and re-accreted with the Mayo Kebbi domain during the Panafrican orogeny. Granite-gneiss rocks of this domain are covered in place by the cretaceous sediments (e.g., the Koum and

Mbéré basins) and by the Cenozoic volcanic rocks of the Cameroon hot line (Figure 1B) [59-61]. The Adamawa-Yadé domain is also characterized by the development of a regional-scale mega-fractures or transcurrent shear zone among which the ENE–WSW-trending Sanaga shear zone (SSZ) and Central Cameroon shear zone (CCSZ) also called the Adamawa fault which extends toward the Gulf of Aden [47-62]. The Central Cameroon shear zone is interpreted as the NW extension of the Pernambuco Fault in NE Brazil [63, 64]. The CCSZ marks the transition between a subdomain with an N–S trending foliation to the north and a subdomain with an E–W-trending foliation to the south [65]. Along the CCSZ shear zone and his Sanaga shear zone relay, kinematic analysis shows an earlier D_2 sinistral transpression followed by a D_3 dextral transtension during the Panafrican Orogeny [47].
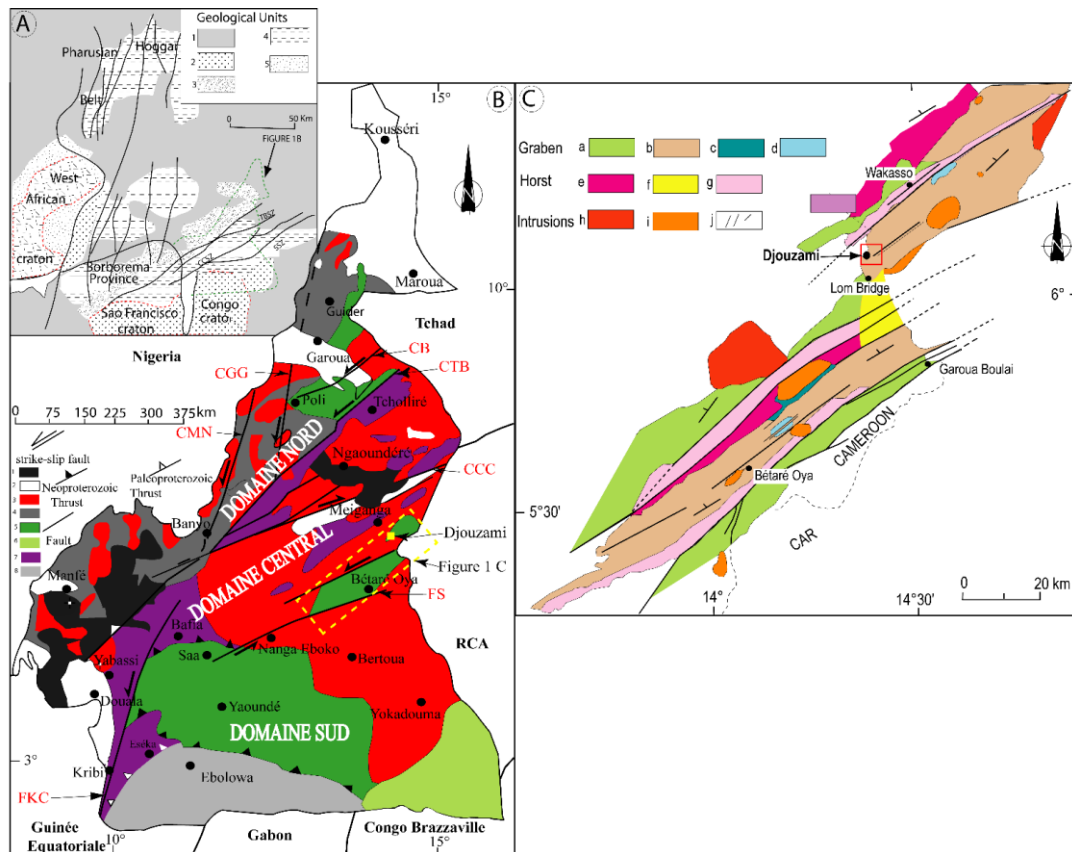

Figure 1. *(A) Geology of West-central Africa and northern Brazil in a Gondwana (pre-drift) reconstruction (modified from [68, 71]. Thick line, boundary of the two continents: (1) Phanerozoic cover; (2) Neoproterozoic formations; (3) Regions of Brasiliano/Panafrican deformation in which Palaeoproterozoic basement is absent or only present as small isolated blocks; (4) Regions of Brasiliano/Panafrican deformation with large amounts of reworked Palaeoproterozoic basement; (5) cratons. (B) Geological map of Cameroon (after [68]. The Lom group is represented by a yellow rectangle. KCF (Kribi-Campo fault); SSZ (Sanaga shear zone); CCSZ (Central Cameroon shear zone); TBSZ (Tcholliré-Banyo shear zone); MNSZ (Mayo Nolti shear zone) and GGSZ (Godé-Gormaya shear zone). (1) volcanic rokcs (Tertiary to recent); (2) Post-Panafrican sedimentary cover; (3) Syn- to Post-tectonic granitoids (500-600Ma); (4) Pre- to syn-tectonic orthogneisses (600-660Ma); (5) Meso- to Neoproterozoic volcano-sedimentary belt (700-1000Ma; (6) Yokadouma and Dja series (age unknown); (7) Palaeoproterozoic gneiss and orthogneiss (2100Ma) and (8) Ntem Complex (3000Ma). (C) Structural map of the Lom Group [72]. Monocyclic units associated to grabens: (a) orthogneiss; (b) Lom volcaniclastic series; (c) polygenic conglomerates; (d) Mari quartzites. Polycyclic units: (e) staurolite micaschists; (f) Lom bridge gneisses; (g) staurolite and chloritoid ductile mylonites. Intrusions with uncertain structural position: (h) granites (G2); (i) granites and monzonites; (j) metalamprophyres (modified after [47]). Inset: location of the Lom Group as an extensional relay zone between two en- echelon segments of the Sanaga fault; the opening of this basin corresponds to sinistral shear movement along these major faults. The study area is indicated in Figure 1C by the red rectangle.*

The Lom group (Figure 1C) consists of metatuffs, volcaniclastic and sedimentary-derived schists, staurolite–garnet micaschists, and quartzites with local conglomerate layers [46]. This group is interpreted as a post-collisional and intra-continental basin developed on the old crust, with depositional age constrained between 613 and 600 Ma [48]. The same works suggest that detrital sources include Archaean to Palaeoproterozoic, late Mesoproterozoic to early Neoproterozoic (1100–950 Ma), and Neoproterozoic (735, 644 and 613 Ma) zircons. The Lom group is characterized by polyphase tectonic evolution with two successive D_1 and D_2 deformations leading to a N50–N70 steeply dipping regional foliation that does not contain any apparent stretching lineation. Dextral or sinistral faults, locally parallel to the main foliation, characterize the later stages of the structural evolution. The associated low-pressure regional metamorphism (garnet–staurolite– andalusite–sillimanite) involved a high thermal gradient related to widespread crustal melting that produced the dominant S-type granitoids in the region [46, 66-68]. The Group is characterized by gold-bearing quartz veins underlining a NE-SW to NNE-SSW-trending shear zone developed during brittle-to-ductile deformation, associated to K‐feldspar alteration and hydrothermal wall‐rock alteration comprising silicification, sericitization, sulphidation, hematitization, and carbonatization [35, 36, 69,70].

3. Methodology

3.1. Ultra-Violet (UV). Fluorescence

The ultra-violet lamp is the high-power U.V lamps in the Blak-Ray B-100 Series which provide bright irradiance for optimal fluorescence. The B-100AP lamp (presented) is placed at the base of the transformer for free-handed operation. The UV method is a method that is used only in the dark environment. As part of our work, we entered the laboratory at night in order to be able to perform our tests in a dark chamber. To make the device work, you must first connect the device to a sector outlet and wait for the lamp to start. Once running, after 60 seconds, we have a purple light that is emitted from the lamp. All that remains is to place the sample to be analyzed under this emitted light and observe. Using a camera, so the flash was disabled, we filmed the samples under the effect of UV. Note that the camera emits ultraviolet radiation for about 3 minutes, then turns off before turning on after 2 minutes in order not to overheat the lamp. You should not expose yourself to this radiation for long because it has harmful effects on the skin and is even a source of cancer.

3.2. Landsat-8 OLI Image Characteristics

The Landsat-8 OLI scene LC08_L1TP_184056_20230212_20230218_02_T1 taken on February 23, 2023, was downloaded free of charge from the United States Geological Survey (USGS) image database at http://earthexplorer.usgs.gov/. The Landsat-8 OLI system, designed by Ball Aerospace Technology, operates from a conventional height of 705 km with an equatorial crossing time of 10 h00 $\pm$ 15 min. It circles the earth every 16 days (except for the highest polar latitude) and has a scene size of 170 km $\times$ 185 km. In general, this system detects geographic information in spectral wavelengths ranging from 0.483 to 2.330 μm, covering the visible to infrared regions. The Landsat-8 OLI image is divided into 11 bands, which include visible (bands 1, 2, and 3), red (band 4), near infrared (band 5), shortwave infrared (bands 6 and 7), panchromatic (band 8), circus (band 9), and thermal (bands 10 and 11). Information capture from the Landsat 8 OLI system is generally at a spatial resolution of 30 m, with the exception of the panchromatic band, which obtains information at 15 m, and the thermal bands, which operate at a spatial resolution of 100 m. Table 1 illustrates the band characteristics of the Landsat OLI system.

Table 1. Landsat-8 OLI image characteristics.

Resolution of Landsat-8 OLI / TIRS			
Band	**Characteristics**	**Spatial resolution**	**Spectral resolution (µm)**
Band 1	Aerosol	30 m $\times$ 30 m	0.433 – 0.453
Band 2	Blue	30 m $\times$ 30 m	0.45 – 0.515
Band 3	Green	30 m $\times$ 30 m	0.525 – 0.6
Band 4	Red	30 m $\times$ 30 m	0.63 – 0.68
Band 5	Near Infrared	30 m $\times$ 30 m	0.845 – 0.885
Band 6	Mid Infrared 1	30 m $\times$ 30 m	1.36 – 1.39
Band 7	Mid Infrared 2	30 m $\times$ 30 m	1.56 – 1.66

Resolution of Landsat-8 OLI / TIRS			
Band	Characteristics	Spatial resolution	Spectral resolution (µm)
Band 8	Panchromatic	15 m × 15 m	0.50 – 0.68
Band 9	Cirrus	30 m × 30 m	2.10 – 2.30
Band 10	Thermal Infrared 1	100 m × 100 m	10.30 – 11.30
Band 11	Thermal Infrared 2	100 m × 100 m	11.50 – 12.50

3.2.1. Pre-treatment of the Landsat-8 OLI Image

Pre-processing mainly consisted of converting digital numbers to reflectance. When acquiring the Landsat 8 image, they take into account the effect of elements obscuring the image. The Landsat-8 OLI image appears with minor radiometric noise and therefore requires less processing. One of the most important processes in mineral exploration and geological discrimination using remote sensing techniques is radiometric correction [73].

In this study, the Haze/Rodiometric and Noise/Reduction modules of Erdas Imagine 2013 software were used to have high dynamic range and contrast. This function refines images using either a tufted cap or a point convolution approach, thus giving real reflectance images of objects on the ground. Image data is calibrated based on radiance, reflectance, or brightness temperatures using radiometric calibration, which reduces errors in the image's digital numbers. Always with the aim of improving the quality of the image, the radiometric correction operation is followed by the atmospheric correction and the geometric correction carried out on ENVIE 5.2. This section focuses on the initial adjustments we used after obtaining the images. Radiometric calibration, atmospheric correction, geometric correction, and noise elimination are the different preprocessing phases. This study uses the atmospheric correction technique to eliminate the effects of the atmosphere on the signal collected by the Landsat 8 satellite sensors. The Fast Line-of-Sight Atmospheric Analysis of Spectral Hypercubes (FLAASH) approach, which is a tool A first-principle atmospheric correction tool that corrects visible, near-infrared, and short-wave infrared wavelengths up to 3 m was employed in this study. Mineral prospecting has benefited from this technology [74-76]. Preprocessing of raw Landsat 8 data, including atmospheric correction, radiometric calibration, and image normalization, was first performed on the dataset before any further processing. In the same environment, image normalization was performed on this dataset.

The main goal of image processing is to obtain a spectral signature of easily detectable hydrothermal alteration of rocks and lineaments. The processing applied in this work consisted of the extraction of the study area and the application of a mask, as well as the improvement of the quality of the images to make them more expressive, allowing better visualization of geological elements and phenomena. This processing includes: the band ratio; principal component analysis (PCA); directional filtering; and lineament extraction.

3.2.2. Treatment of Landsat-8 OLI Image

(i). Bands Ratio

Band ratio analysis is a technique that relies primarily on selected band operations. It is widely used and applied to mineral exploration to detect hydrothermal alterations that may be linked to mineral deposits [20, 77]. The band ratio consists of combining information from multiple bands into one. The band ratios that will be performed are: iron oxides, Al-OH-rich rocks, clay minerals, and hydrothermal alteration. In general, the ratio analysis bands are essential to highlight specific features that are not visible on individual bands, and the selection of the most appropriate bands for ratio analysis depends on the spectral properties of the rock or minerals and their relative abundance [78]. The band ratio statistic can be calculated by dividing the digital number of a given band by the digital number of another band. Equation (1) illustrates the basic equation of band ratio analysis [79].

$$Br = \frac{(B1)_i}{(B2)_j} \qquad (1)$$

Where B1 and B2 are the specific bands, and i and j represent the digital numbers in these bands. In this study, the 6/7, 6/5, and 4/2 band ratios of Landsat 8 OLI imagery were used to highlight hydrothermal alterations.

(ii). Principal Component Analysis (PCA)

Principal Component Analysis (PCA) is a mathematical transformation that consists of calculating the eigenvalues and eigenvectors of the variance-covariance matrix calculated from a series of images, then the principal components of the numerical count of the multi-spectral bands [80-82]. It is a multivariate statistical analysis that aims to transform correlated variables into new free variables (principal components). PCA is very important for unraveling alteration evidence that may represent mineralization patterns [20, 25, 83]. Basically,

PCA transforms several correlated spectral bands into a smaller number of uncorrelated spectral bands called principal components. In exploration studies, PCA has been applied to Landsat imagery [84, 85]. In this study, PCA was applied to Landsat bands (2–7) to improve information relating to hydrothermal alterations, associated mineralizations, and to extract lineaments.

3.2.3. Lineaments Extraction

This treatment is applied to the ACP1 component [86]. It involves the application of directional filters (N-S, E-W, NE-SW, and NE-SW) using the 7×7 Sobel matrix (Table 2). It makes it possible to highlight the major directions of linear structures. The filtering method is a technique aimed at eliminating noise con-

tained in satellite data [87, 88]. This technique makes it possible to improve the visual quality of the image in order to facilitate its interpretation. In geology, we are interested in discontinuities in textures such as the contours of relatively homogeneous zones, which can reveal the presence of faults or fractures [89]. Enhancement of lineaments amounts to highlighting in the image the strong reflectance transitions (tonal and/or texture contrast) in the image and the high spatial frequencies that are generally associated with them. Directional filters improve the perception of lineaments by causing an optical shadow effect to cast on the image as if it were illuminated by grazing light [90]. In addition, this type of filter makes it possible to enhance lineaments (Table 3) that are not favored by the lighting source.

Table 2. 7×7 matrix of Sobel.

N-S							NE-SW						
-1.0	-1.0	-1.0	0.0	1.0	1.0	1.0	-1.0	-1.0	-1.0	-1.0	-1.0	-1.0	-1.0
-1.0	-1.0	-1.0	0.0	1.0	1.0	1.0	-1.0	-1.0	-1.0	-1.0	-1.0	-1.0	-1.0
-1.0	-1.0	-1.0	0.0	1.0	1.0	1.0	-1.0	-1.0	-1.0	-1.0	-1.0	-1.0	-1.0
-1.0	-1.0	-1.0	0.0	1.0	1.0	1.0	0.0	0.0	0.0	0.0	0.0	0.0	0.0
-1.0	-1.0	-1.0	0.0	1.0	1.0	1.0	1.0	1.0	1.0	1.0	1.0	1.0	1.0
-1.0	-1.0	-1.0	0.0	1.0	1.0	1.0	1.0	1.0	1.0	1.0	1.0	1.0	1.0
-1.0	-1.0	-1.0	0.0	1.0	1.0	1.0	1.0	1.0	1.0	1.0	1.0	1.0	1.0
E-W							NW-SE						
0.0	0.0	0.0	-0.7	-1.4	-1.4	-1.4	-1.0	-1.0	-1.0	0.0	1.0	1.0	1.0
0.0	0.0	0.0	-0.7	-1.4	-1.4	-1.4	-1.0	-1.0	-1.0	0.0	1.0	1.0	1.0
0.0	0.0	0.0	-0.7	-1.4	-1.4	-1.4	-1.0	-1.0	-1.0	0.0	1.0	1.0	1.0
1.4	1.4	1.4	0.0	-0.7	-0.7	-0.7	-1.0	-1.0	-1.0	0.0	1.0	1.0	1.0
1.4	1.4	1.4	0.7	0.0	0.0	0.0	-1.0	-1.0	-1.0	0.0	1.0	1.0	1.0
1.4	1.4	1.4	0.7	0.0	0.0	0.0	-1.0	-1.0	-1.0	0.0	1.0	1.0	1.0
1.4	1.4	1.4	0.7	0.0	0.0	0.0	-1.0	-1.0	-1.0	0.0	1.0	1.0	1.0

Table 3. Software specification for lineament extraction.

Sn	Parameter Settings	Parameter Value
1	Filter Radius (Pixels)	5
2	Edge Gradient Threshold	10
3	Curved Length Threshold (Pixels)	10
4	Line fitting Error Threshold (Pixels)	3
5	Angular difference Threshold (Degrees)	30
6	Linking Distance Threshold (Pixels)	20

3.2.4. Control and Validation of Mapping Results

Satellite image processing regularly faces the problem of the reliability of the results it offers and their validation [91-93]. This highlights the need to carry out control and validation of all results of the interpretation of derived images. After any satellite image processing, geologists regularly encounter the problem of the reliability of the results they propose and their validation [91-93]. This supports the obligation to carry out control and validation of all results of the interpretation of processed images. This evaluation and validation phase is very essential for a mapping study of the lineaments in the base zone, given the complexity of this environment. For a substantial improvement in the results obtained as part of this study, several verification and validation missions in the field were carried out. The phase of evaluation and validation of the lineaments extracted from the digital processing of satellite

images is essential to judging the relevance of the method used [94-97].

The lineaments identified from Landsat-8 OLI images were the subject of a frequency analysis to highlight the main directions. To validate these lineaments, the directions obtained are then compared to those of previous work carried out in the study area [98-101]. The structural diagram obtained also complements the inventory of faults in this area. The lineaments mapped by satellite imagery and retained as part of this study will have a fracturing value and could be assimilated to fractures or tectonic discontinuities. When the anthropogenic origin of a linear structure has been proven (roads, tracks, limits of forests or cultivated areas, high voltage lines, etc.), it has been removed. Thus, those remaining must probably correspond to tectonic fracturing [102-105].
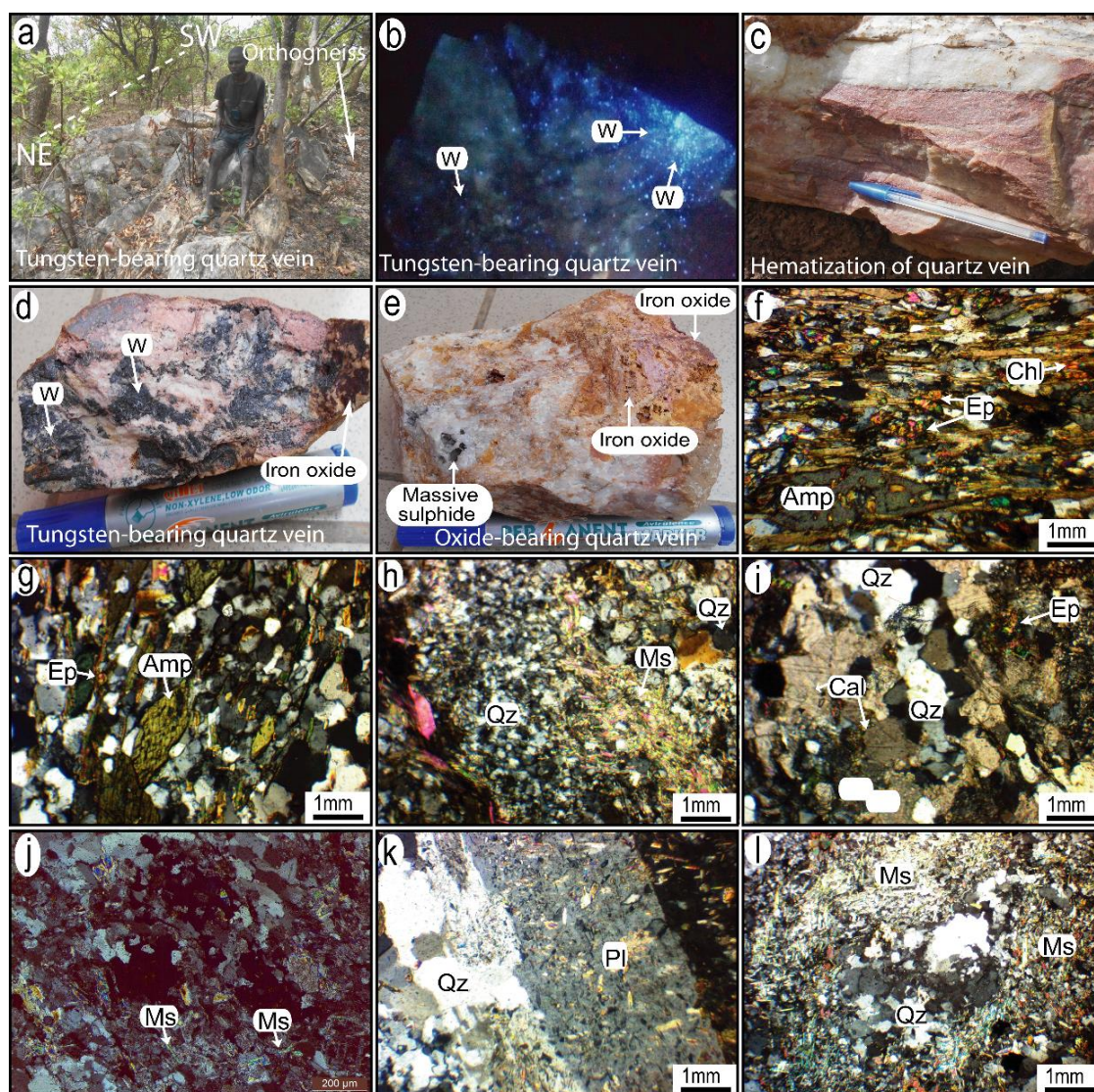

Figure 2. *Photography and microphotography of the rocks from Djouzami. (a) tungsten-bearing quartz vein with NE-SW trends, cross-cutting orthogneiss; (b) Blue fluorescence of tungsten (scheelite) in the quartz vein sample; (c) Hematization of quartz vein; (d) Tungsten (scheelite)-iron oxide association in the quartz vein sample; (e) Massive sulphide-iron oxide association in the quartz vein sample; (f, g) Epidote and chlorite Hydrothermal in amphibolite; (h, i) Muscovite-epidote-calcite Hydrothermal in orthogneiss; (j) Muscovitization in mylonitic gneiss; (k) Sericitization in metagranite; (l) Muscovitization in metagranite.*

4. Results

4.1. Ultra-Violet Fluorescence Data and Hydrothermal Mineral Associations

On the field, tungsten (scheelite)-bearing quartz veins cross cut amphibolites, orthogneiss, mylonitic gneisses, and meta-granites (e.g., Figure 2a). Scheelite is recognized in quartz veins by its blue luminescence under ultra-violet lighting (Figure 2b).

Hydrothermal alterations related to this mineralization affect the host rock in the study area progressively, depending on their mineralogical composition and structure. The main hydrothermal alterations process recognized in the mineralized quartz veins are hematization and tourmalinization (Figure 2c). By contrast in the host rocks, hydrothermal alteration types include clay/carbonate alterations, phyllic (sericite and muscovite) alterations, prophyllic (epidote and chlorite) alterations, potassic (K-feldspar) alterations, as well as silicification and sulfidation (Figures. 2h, i, j, k, l). Phyllic, clayey/carbonate, and prophyllic alterations are predominant in the distal alteration zone. Phyllic alteration and carbonatation are closely related to tungsten mineralization, and they are abundant in the proximal alteration zones (Figures 2d, e). Prophyllic alteration are abundant in amphibolites, and it is widespread around most tungsten ore veins, extending up to several meters from the ore body with a gradually decreasing intensity of development. Pyrite; iron oxide, sericite, and apatite are common in this zone. Phyllic alteration (sericite and muscovite) is dominated in orthogneiss, mylonitic gneiss, and metagranites (Figures 2h, i, j, k, and l). Muscovite is one of the most predominant types of hydrothermal alteration mineral in orthogneiss.

4.2. Mapping of Hydrothermal Alterations

The hydrothermal alteration zones in the Djouzami area are shows on the map of Figure 3. This map display the zones of abundance of iron oxides (Figure 3a), the zones of abundance of ferrous minerals (Figure 3b), the zones of abundance of clay and carbonate minerals (Figure 3c), and the zones of hydrothermal alteration (Figure 3d).

The Landsat 8 image band ratio method was applied to create combined RBG images highlighting hydrothermally altered rocks. The ratio of band 4 and band 2 was applied to highlight areas where iron oxide/hydroxide-containing minerals are abundant (Figure 3a), as bright red-toned pixels, which are concentrated in the alteration zones associated with tungsten and gold mineralization (Figure 3a). Average concentrations are present throughout the study area, with the exception of the eastern part of our study sector. The 6/5 band ratio makes it possible to distinguish ferrous minerals in a bright tone and shows a strong reflectance, indicating the presence of ferrous minerals in the form of a red pixel in the zones mineralized in tungsten and gold (Figure 3b). The 6/7 band ratio makes it possible to distinguish altered rocks containing clay minerals Al-OH, (Fe, Mg) –OH and carbonate minerals in darker blue pixels (Figure 3c). Average concentrations are very poorly dispersed in the entire study area, while the highest concentrations are limited to a few key locations. This ratio of band 6 and band 7 was used to map areas of clay minerals, shown in blue, but it is also sensitive to moisture variations in vegetation and soils, which also highlights vegetation.

RGB composite images containing band ratios were produced. An image using the ratio of Sabin (1999) (4/2, 6/7, 6/5) was calculated for mapping the identification of hydrothermal alteration zones (Figure 3d). By superimposing that sites where at least two types of mineralization meet are likely to be subject to the flow of hydrothermal minerals, The areas in purple, red, and blue concentrated in the central, western, and south-western parts of Djouzami are identified as areas with high potential for unexploited tungsten and gold mineralization, which could be good prospects for future detailed exploration (Figure 3d). The distribution of minerals in the study area is mainly found in areas crossed by tungsten veins or near gold occurrences. The minerals concentrate most strongly in the central part of the study area and form elongated bodies along the NE-SW direction (Figure 3d). Hydrothermal alteration zones highlight relationships between them.
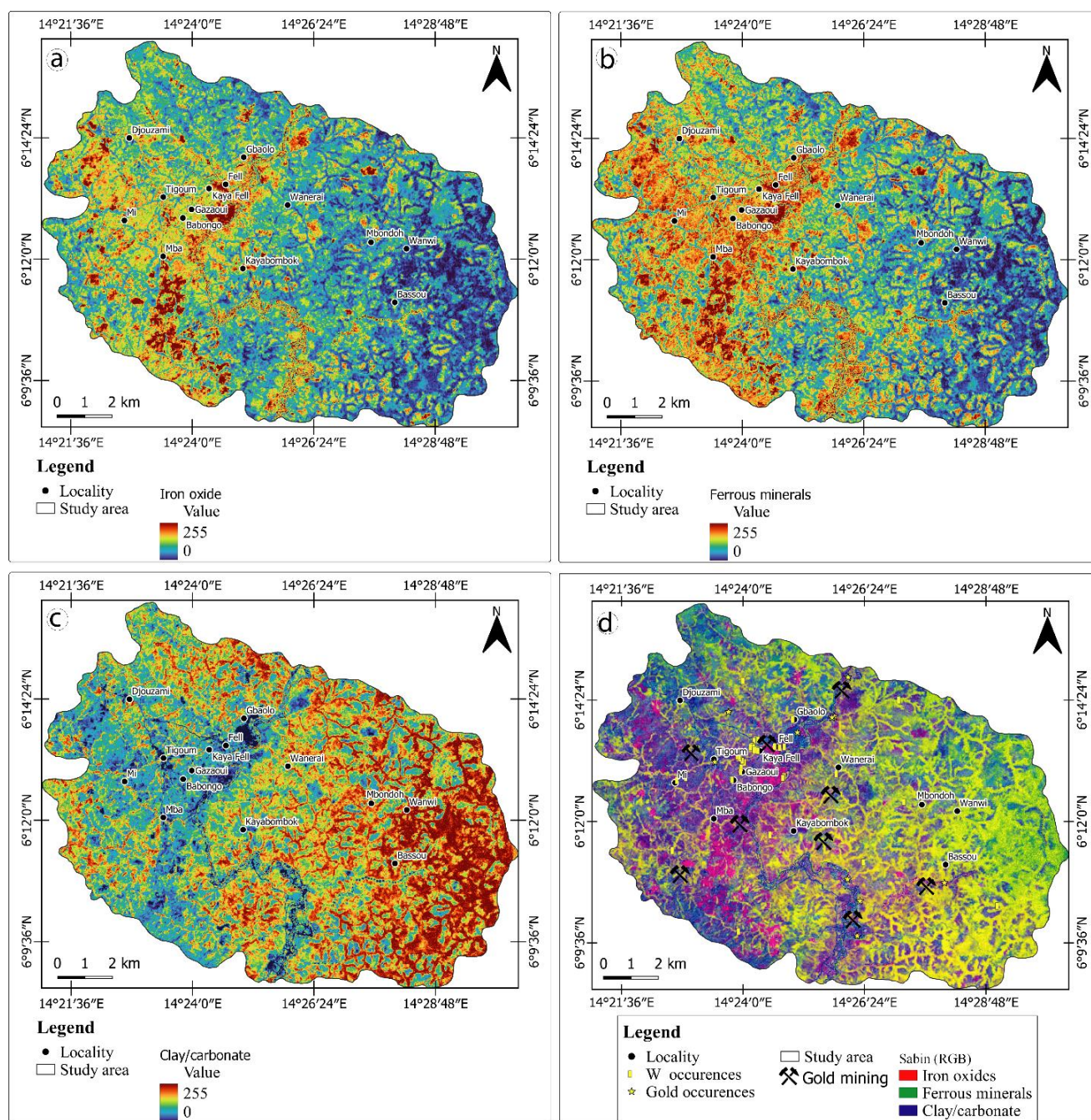
Figure 3. *Map of the hydrothermal alteration zones from the Djouzami (extract from the Landsat 8 image). (a) Map showing areas of abundance of iron oxides; (b) Map showing areas of abundance of ferrous minerals; (c) Map showing areas of abundance of clay and carbonate minerals; (d) Map from the Sabin 1999 report showing zones of hydrothermal alteration.*

4.3. Extraction and Analysis of Lineaments

Principal component analysis (PCA), image combinations and directional spatial filtering were applied for image enhancement (Figure 4).
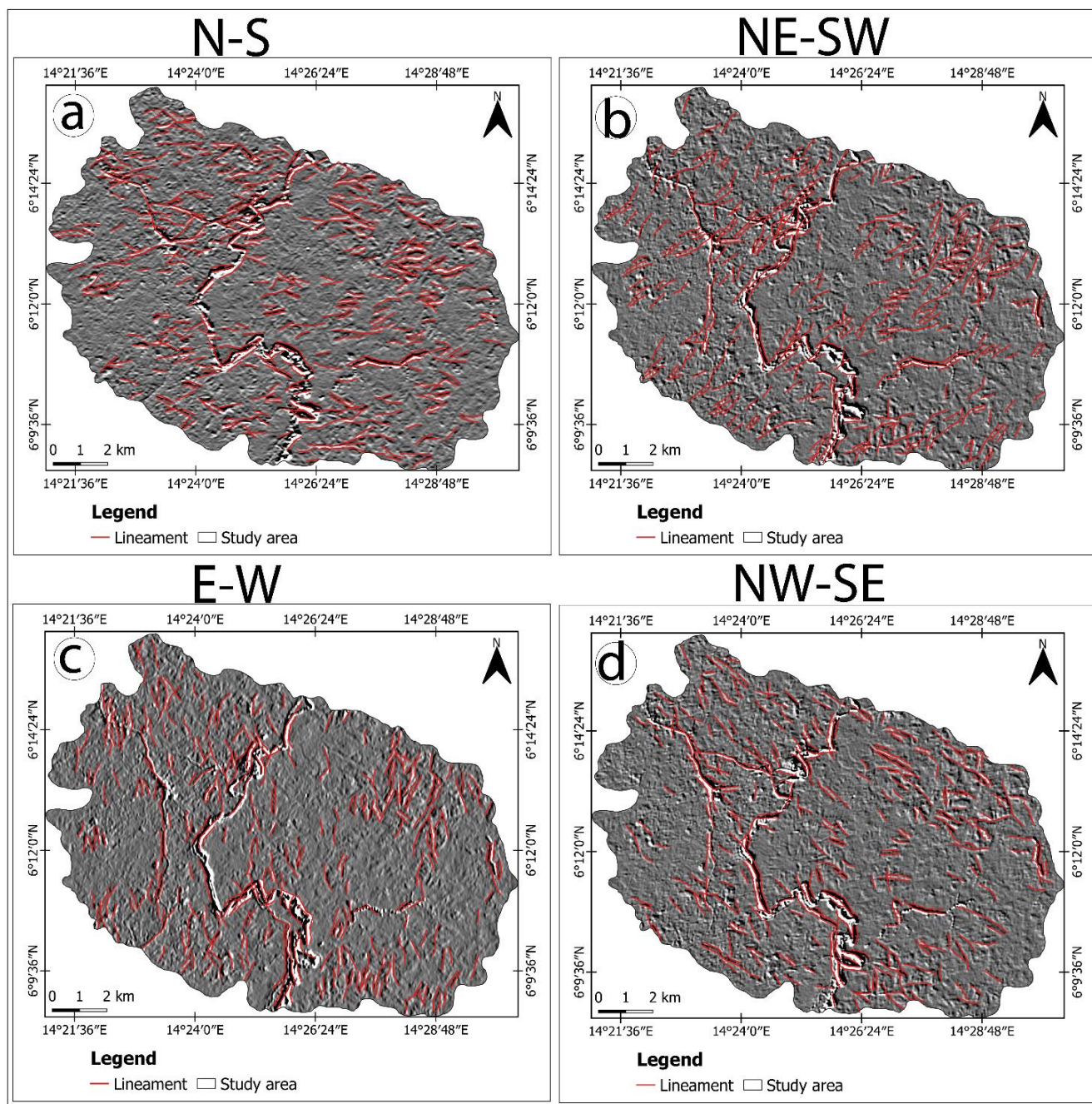
Figure 4. Sobel directional filter map of Djouzami lineaments (extracted from Landsat 8, ACP1 image). (a) Directional Sobel filter map of N-S lineaments; (b) Directional Sobel filter map of NE-SW lineaments; (c) Directional Sobel filter map of E-W lineaments; (d) Directional Sobel filter map of NW-SE lineaments.

Lineaments represent linear geological objects or alignments of sufficiently close geological objects, topographic discontinuities, or geomorphological structures inherited from ancient topographies [88]. On the figure 4, the lineaments are materialized by the limits formed by the dark and light areas. They can sometimes extend over several kilometers. The different results presented in figure 4 more or less clearly enhance the lineaments of the sector. The detailed map of the lineaments (Figure 4) was produced thanks to an interpretation of the images derived from the different processing techniques. This map presents a significant density of lineaments of varying sizes, ranging from a few hundred meters to several kilometers. The N-S directional filter applied to ACP1 allowed the extraction of 394 lineaments (Figure 4a). The directions of the lineaments obtained from this filter were processed into directional rosettes, in order to evaluate their distribution (Figure 5).
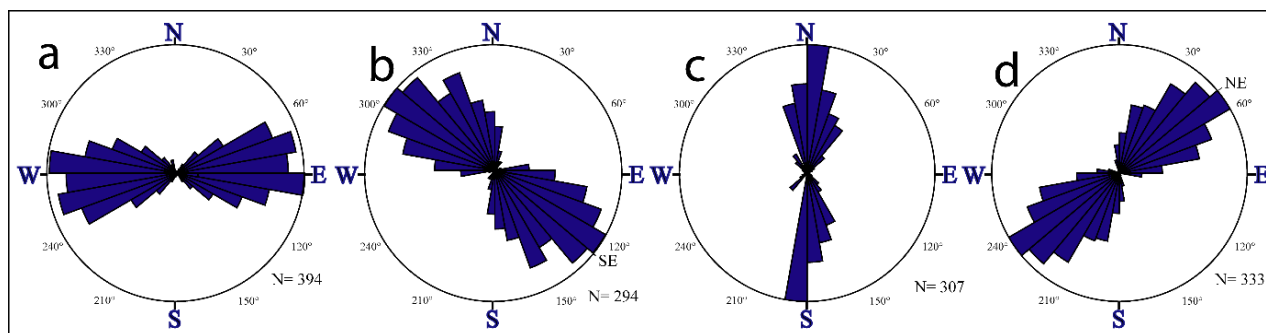
Figure 5. Rose direction diagram of Djouzami Sobel directional filter lineaments. (a) Rose diagram of N-S lineaments; (b) Rose lineament diagram; (c) Rose diagram of E-W lineaments; (d) Rose diagram of NW-SE lineaments.

In Figure 5, the main direction is WNW-ESE and the secondary one is ENE-WSW (Figure 5a). The lineaments by Sobel NE-SW directional filter (Figure 4b) applied ACP1; this filter allows the extraction of 294 lineaments whose major direction is NW-SE and the secondary one NNW-SSE (Figure 5b). The lineaments by the Sobel E-W directional filter, applied to ACP1, allow the extraction of 307 lineaments (Figure 4c) and make it possible to highlight the directions following N-E and NE-SW (Figure 5c). The lineaments by the Sobel NW-SE directional filter applied to ACP1 allow the

extraction of 333 lineaments (Figure 4d), the major direction of which is NE-SW (Figure 5d).

4.4. Combination of Sobel Filter Lineaments

A total of 1334 lineaments were highlighted by filtering the ACP1 image on the 7×7 Sobel window, following the directions N-S, NE-SW, E-W, and NW-SE. The combination map of the lineaments highlights the sector crossed by the bed of the Lom River as being the most fractured (Figure 6).
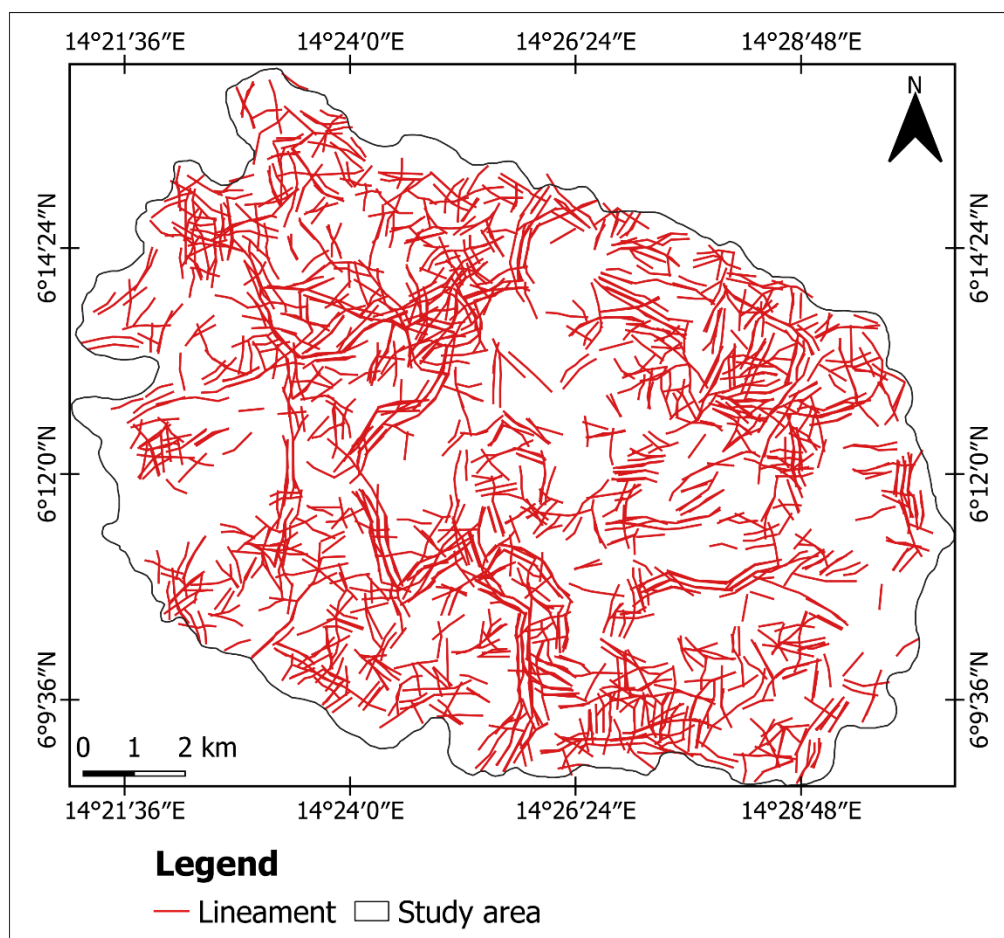

Figure 6. Summary map of lineaments from Djouzami.

The lineaments present a more continuous cartographic layout. These lineaments are characterized by more accentuated cartographic continuity and looser spatial density and therefore represent the fracturing of the study area. In order to study the geometry of the lineament network and identify the dominant directions, a statistical analysis was carried out. The main directions of the mapped lineaments are between ENE-WSW, N-S, and NE-SW (Figure 7).
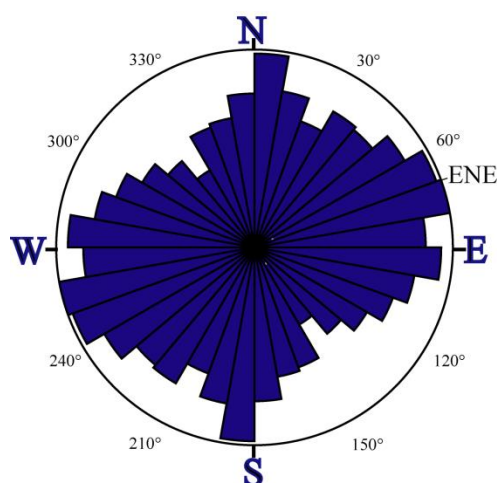

Figure 7. Rose summary diagram of the direction of Djouzami lineaments.

5. Discussion

Previous works have reported occurrences of rare metal mineralizations in several areas of Eastern and Adamawa Cameroon [35, 36]. Into quartz veins which cross cut metamorphic rocks (orthogneiss, amphibolite, mylonitic gneiss and metagranite) in the Djouzami area, minerals characterized by the blue luminescence on the ultra-violet fluorescence corresponds to tungsten (scheelite). Scheelite related to veins in the French Massif central and to granite intrusion of Pyrenees is characterized by this typical blue luminescence [106, 107]. Most mineral deposits are identify in the field by recognizing surface rocks that have undergone hydrothermal alteration [108-114]. Some type of hydrothermal alterations can be better distinguished through remote sensing than in the field or through petrographic study, as most minerals have absorption characteristics at wavelengths outside the spectrum visible to the human eye [20, 77, 79]. In the Djouzami area, interaction between hydrothermal fluids and silicates of the host rock induce mineralogical transformations, giving rise to neoformed minerals associated with metallic minerals, tungsten, and probably gold mineralization. The study area is characterized by the high-intensity hydrothermal alteration, which damaged many rocks. The hydrothermal minerals assemblage made of chlorite, epidote, muscovite and/or sericite, hematite, tourmaline, as well as opaque minerals are associated to tungsten in the quartz veins. This assemblage is comparable to the one accompanying scheelite-related to quartz veins reported in the French Variscan range of the Massif Central and in Portugal [115, 25]. Based on the reflectance spectrum of minerals, whose numerous absorption-feature wavelengths are characterized within the VNIR and SWIR ranges, a number of authors have conducted studies pertaining to the groups of alteration minerals (oxides, clays, and carbonates) in hydrothermal alteration areas [116, 117]. According to [118], these minerals can be identified by the spectrum difference between their unique absorptions in altered rocks that have undergone hydrothermal alteration. With regard to the mineralogy of the altered rocks and the spectral resolution of the OLI sensor, it is noted that rock containing clays, carbonates, and chloritic elements exhibit a greater spectral gradient in Landsat 8 bands 6 and 7 (SWIR range) (Figure 5). Due to the main absorption features in the visible to NIR spectral region, derived from ferric iron, the iron oxides and hydroxyl enrichment of the mineralized altered rocks (e. g., hematite) are derived from the supergene activity that affects other hydrothermal minerals such as pyrite. These minerals have served as spectral indicators for targeting tungsten exploration. But it should also be noted that the hydrothermal alteration process described in the Djouzami area are identical to those of the gold mineralization described in rocks of the Lom group [20, 55, 119], and they accompany tungsten (scheelite) mineralization.

Lineament analysis can provides a valuable framework to guide the early stages of tungsten exploration in the Djouzami area. On the map of figure 6, most of the lineaments have curvilinear trajectories which indicates their penetrative character and suggests that they correspond to regional foliations. These lineaments have various trending, the main directions being ENE-WSW, NE-SW, N-S and E-W (Figure 7). The lineaments trended ENE-WSW are concordant to the well-known regional geological structures in southern Cameroon namely the Sanaga shear zone [47, 48, 53, 64, 65, 120, 121]. The N-S lineaments corresponds to foliation reported in granitic rocks south of Meiganga area [72]; the E-W trending lineaments are equivalent to the foliation in gneiss and orthogneiss from Meiganga area [122]. The NE-SW trending lineaments are concordant to the N040E Djouzami shear zone, the NE-SW trending Meiganga shear zone and the N050 mylonitic band which underline globally the Lom group [47, 53, 122]. The lineaments characterized by the NE-SW trends are concordant to the direction of the tungsten-bearing quartz veins and the regional foliation (e. g. Figure 3a, b). In addition, the map of tungsten indices reveals a clear correlation between areas with high tungsten potential and high lineament density (oriented NE-SW). This association suggest that the NE-SW trending shear zone in the study area correspond to a channel for tungsten fluid flow or that it control tungsten mineralization. The Djouzami shear zone trends NE-SW similarly to the Bétaré-Oya shear zone (Just southwest of the

study area) which structurally controls gold-bearing quartz veins [123-126]. It is underlined in the Djouzami area by mylonitic foliation [47]. and on the field, this foliation is often delineated by quartz veins (Figure 3a) suggesting that is correspond to brittle-ductile shear zone. According to some researchers, brittle-ductile shear zones are the preferential setting for metals concentration such as mesothermal orogenic gold mineralization [127, 128]. In several metalliferous districts, they are association between tungsten and gold mineralization [106, 107]. As hydrothermal mineral assemblage identified in this study is similar to the one accompanying gold mineralization in the Lom group [37, 70], it is no excluded that the Djouzami shear zone control both gold and tungsten. Were also able to establish a positive correlation between lineamentary geological structures and existing mineralization using Landsat 8 imagery in the tropics. The results on the lineament aspect, interconnections between lineaments, and fracturing density of the study area are consistent with the work of [129]. The Paddington tungsten hydrothermal veins deposit in Australia and the Ajjanahalli deposit in India are also controlled by major fractures [130-132].

6. Conclusions

The Djouzami area in the Adamawa-Yadé domain is dominantly made of metamorphic rocks, cross cut in place by mineralized quartz veins. Integrated ultra-violet fluorescence and remote sensing using Landsat-8 OLI images have led to the following specific conclusions:

1. Tungsten (scheelite) mineralization is hosted in quartz veins and it is characterized by its blue luminescence under ultra-violet lighting. The hydrothermal minerals assemblage accompanying this mineralization is made of muscovite, chlorite, tourmaline, hematite, calcite and sericite, similar to the gold-bearing quartz veins reported in the Lom group. The metallic minerals include only pyrite.
2. Alteration minerals mapped by remote sensing through study band ratios 6/7, 4/2 and 6/5 are respectively clay, iron oxide/hydroxides, and ferrous minerals. Lineaments mapped corresponds to regional foliations and/or shear zones and they are trended following the ENE-WSW, NE-SW, N-S and E-W directions.
3. The high hydrothermal zones and tungsten-bearing quartz veins are located along the NE-SW shear zone. This geological structure is considered as the pathway for mineralizing fluids and ground water circulation, and control tungsten mineralization.

Abbreviations

OLI	Operational Land Imager
PCA	Principal Component Analysis
BR	Band Ratio
VNIR	Visible Infrared Imaging Radiometer Suite
SWIR	Short-Wave Infrared
FLAASH	Fast Line-of-Sight Atmospheric
USGS	United States Geological Survey
TIRS	Thermal Infrared Sensor
RBG	Red Bleu Green
NIR	Near Infrared
W	Tungsten

Author Contributions

Yingyang Wanbitching Raoul: Conceptualization, Data curation, Formal Analysis, Funding acquisition, Investigation, Methodology, Project administration, Resources, Software, Writing – original draft, Writing – review & editing

Nomo Negue Emmanuel: Project administration, Resources, Supervision, Validation, Visualization

Nguihdama Dagwaï: Funding acquisition, Investigation, Project administration, Resources

Ayiwouo Ngounouno Mouhamed: Formal Analysis, Funding acquisition, Methodology, Investigation

Mbohou Mgambié Isaac Bertrand: Project administration, Supervision, Validation, Visualization

Ngounouno Ismaïla: Project administration, Supervision, Validation, Visualization

Conflicts of Interest

The authors declare no conflicts of interest.

References

[1] Černý P, Ercit TS. The classification of granitic pegmatites revisited. (2005), Can Mineral 43. http://dx.doi.org/10.2113/gscanmin.43.6.2005

[2] Romer RL, Kroner U. Phanerozoic tin and tungsten mineralization—Tectonic controls on the distribution of enriched protoliths and heat sources for crustal melting. (2016), Gondwana Res 31: 60–95, https://doi.org/10.1016/j.gr.2015.11.002

[3] Legros H, Harlaux M, Mercadier J, Romer RL, Poujol M, Camacho A. The world-class Nanling metallogenic belt (Jiangxi, China): W and Sn deposition at 160 Ma followed by 30 my of hydrothermal metal redistribution. (2020), Ore Geology Reviews 117: 103302 (Chine). Sciences de la Terre. Université de Lorraine. https://doi.org/10.1016/j.oregeorev.2019.103302

[4] Polya DA, Foxford KA, Stuart F, Boyce A, Fallick AE. Evolution and paragenetic context of low δD hydrothermal fluids from the Panasqueira W-Sn deposit, Portugal: Etat de l'art 36 new evidence from microthermometric, stable isotope, noble gas and halogen analyses of primary fluid inclusions. (2000), Geochim Cosmochim Acta 64: 3357-3371. https://doi.org/10.1016/S0016-7037(00)00459-2

[5] Cheval-Garabédian F, Faure M, Marcoux E, Gouin J, Picault M. The La Bellière gold and antimony district (French Armorican Massif): a two-stage evolution model controlled by Variscan strikeslip tectonic. (2020), Ore Geol Rev 125: 103–681. https://doi.org/10.1016/j.oregeorev.2020.103681

[6] Matthieu Harlaux, Christian Marignac, Julien Mercadier, Marc Poujol, Marie-Christine Boiron, Kalin Kouzmanov, Alfredo Camacho, Saïda Alikouss, Benjamin Roméo, Bernard Mouthier and Michel CuneyMultistage development of a hydrothermal W deposit during the Variscan late-orogenic evolution: the Puy-les-Vignes breccia pipe (Massif Central, France). 2021. BSGF - Earth Sciences Bulletin, 192, 33. https://doi.org/10.1051/bsgf/2021023

[7] Qiangwei Su, J Mao, J Sun, Zhao L, Xu S. Geochemistry and origin of scheelites from the Xiaoyao tungsten skarn deposit in the Jiangnan tungsten belt, SE China. (2020), Minerals. https://doi.org/10.3390/min10030271

[8] Melleton JEF et Gloaguen E. Les techniques d'exploration minière utilisées pour la recherche de l'or. 2018, Bureau de recherches géologiques et minières (BRGM). Réalités industrielles - annales des mines. http://dx.doi.org/10.3917/rindu1.184.0005

[9] Van Ruitenbeek FJA, Cudahy TJ, Van der Meer FD, Hale M. Characterization of the hydrothermal systems associated with Archean VMS – mineralization at Panorama, Western Australia, using hyperspectral, geochemical and geothermometric data. (2012), Ore geology reviews 45: 33–46. https://doi.org/10.1016/j.jag.2011.08.002

[10] Petrovic A, Khan SD, Thurmond AK. Integrated hyperspectral remote sensing, geochemical and isotopic studies for understanding hydrocarbon-induced rock alterations. (2012), Mar Pet Geol 35: 292–308. http://dx.doi.org/10.1016/j.marpetgeo.2012.01.004

[11] Shi P, Fu B, Ninomiya Y, Sun J, Li Y. Multispectral remote sensing mapping for hydrocarbon seepage-induced lithologic anomalies in the Kuqa foreland basin, south Tian Shan. (2012), J Asian Earth Sci 46: 70–77. http://dx.doi.org/10.1016/j.jseaes.2011.10.019

[12] Lammoglia T, Filho CRS. Spectroscopic characterization of oils yielded from Brazilian offshore basins: Potential applications of remote sensing. (2011), Remote Sens Environ 115: 2525–2535. http://dx.doi.org/10.1016/j.rse.2011.04.038

[13] Aminzadeh B, Samani F. Identifying the boundaries of the historical site of Persepolis using remote sensing. (2006), Remote Sens Environ 102: 52–62. http://dx.doi.org/10.1016/j.rse.2006.01.018

[14] Watts, D., Harris, N. Mapping granite and gneiss in domes along the North Himalaya antiform with ASTER SWIR band ratios. (2005), Geological Society of America Bulletin. v. 117(7-8), p. 879-886. https://doi.org/10.1130/B25592.1

[15] Vaughan RG, Hook SJ, Calvin WM, Taranik JV. Surface mineral mapping at Steamboat Springs, Nevada, USA, with multi-wavelength thermal infrared images. (2005), Remote Sens Environ 99: 140–158. http://dx.doi.org/10.1016/j.rse.2005.04.030

[16] Galvão, L. S., Almeida-Filho, R., Vitorello, I. Spectral discrimination of hydrothermally altered materials using ASTER short-wave infrared bands: evaluation in a tropical savannah environment. (2005), Int. J. Appl. Earth Obs. Geoinformation 7, 107–114. http://dx.doi.org/10.1016/j.jag.2004.12.003

[17] Hellman MJ, Ramsey MS. Analysis of hot springs and associated deposits in Yellowstone National Park using ASTER and AVIRIS remote sensing. (2004), J Volcanol Geotherm Res 135: 195–219. https://doi.org/10.1016/j.jvolgeores.2003.12.012

[18] Kucukkaya AG. Photogrammetry and remote in archeology. (2004), J Quant Spectroscopy Radiative Transf 88: 83–88. http://dx.doi.org/10.1016/j.jqsrt.2003.12.030

[19] Takodjou Wambo JD, Ganno S, Djonthu Lahe YS, Kouankap Nono GD, Fossi DH, Tchouatcha MS, Nzenti JP. Geostatistical and GIS analysis of the spatial variability of alluvial gold content in NgouraColomines area, Eastern Cameroon: Implications for the exploration of primary gold deposit. (2018), J Afr Earth Sci 142: 138–157. https://doi.org/10.1016/j.jafrearsci.2018.03.015

[20] Takodjou, W. J. D., Pour, A. B., Ganno, S., Asimow, P. D., Zoheir, B., Salles, R. d. R., Muslim, A. M. Identifying high potential zones of gold mineralization in a sub-tropical region using Landsat-8 and ASTER remote sensing data: A case study of the Ngoura-Colomines goldfield, eastern Cameroon. (2020), Ore Geology Reviews, 122, 103530. https://doi.org/10.1016/j.oregeorev.2020.103530

[21] Ketchaya, Y. B., Dong, G., Santosh, M., & Lemdjou, Y. B. Microchemical signatures of placer gold grains from the Gamba district, northern Cameroon: Implications for possible bedrock sources. (2022), Ore Geology Reviews, 141, 104640. https://doi.org/10.1002/gj.4197

[22] Sabins F. Remote sensing for mineral exploration. (1999), Ore Geol Rev 14: 157–183. https://doi.org/10.1016/S0169-1368(99)00007-4

[23] Rajesh HM. Application of remote sensing and GIS in mineral: ressource mapping-and overview. (2004), J Mineral Petrol Sci 99(3): 83–103. https://doi.org/10.2465/jmps.99.83.

[24] Moradi M, Basiri S, Kananian A, Kabiri K. Fuzzy logic modeling for hydrothermal gold mineralization mapping using geochemical, geological, ASTER imageries and other geo-data, a case study in Central Alborz, Iran. (2014), Earth Sci Inf 8: 197–205. https://doi.org/10.1007/s12145-014-0151-9

[25] Frutuoso, R.; Lima, A.; Teodoro, A. C. Application of remote sensing data in gold exploration: Targeting hydrothermal alteration using Landsat 8 imagery in northern Portugal. (2021), Arab. J. Geosci. 14, 1–18. 6. https://doi.org/10.1007/s12517-021-06786-0

[26] Anaba Fotze, Q. M., Bikoro Bi-Alou, M., Ndougsa-Mbarga, T., Bailly, L., Bernard, J., Penaye, J., Sep Nlomngan, J. P., Djieto Lordon, A. E., Ketchaya, Y. B., & Moussango Ibohn, P. A. Integrating Aster 07XT, Landsat 8, and aeromagnetic data for the delineation of potential mineralization sites in North Cameroon. (2022), Geological Journal, 1–23. https://doi.org/10.1002/gj.4513

[27] Pour, B. A., Hashim, M., a Marghany, M. Exploration of gold mineralization in a tropical region using Earth Observing-1 (EO1) and JERS-1 SAR data: a case study from Bau gold field, Sarawak, Malaysia. (2014). Arabian Journal of Geosciences 7(6), 2393-2406. https://doi.org/10.1007/s12517-013-0969-3

[28] Tohid Y, Farhang A, Ali A, Ali AC. Integrating geologic and Landsat-8 and ASTER remote sensing data for gold exploration: a case study from Zarshuran Carlin-type gold deposit, NW Iran. (2018), Arabian Journal of Geosciences 11: 482 https://doi.org/10.1007/s12517-018-3822-x

[29] Danra Moh Guela Guy Basile, Tchameni Rigobert, Daouda Dawa ï Fosso Tchunte Periclex Martial, Awé Salomon, and Bisségué Jean Claude. "Geological Mapping of the Panafrican Mokong Gneisess and Granitoides (Far North Cameroon): Contribution of SEMI-automatic Processing from Landsat 8 OIL/TIRS Images. (2019), Journal of Geosciences and Geomatics, vol. 7, no. 2: 80-87. https://doi.org/10.12691/jgg-7-2-4

[30] Bolouki SM, Ramazi HR, Maghsoudi A, Pour AB, Sohrabi G. A remote sensing-based application of Bayesian networks for epithermal gold potential mapping in Ahar-Arasbaran area, NW Iran. (2020), Remote Sens 12: 105. https://doi.org/10.3390/rs12010105

[31] Mahboob MA, Genc B, Celik T, Ali S, Atif I. Mapping hydrothermal minerals using remotely sensed reflectance spectroscopy data from Landsat. Journal of the Southern African Institute of Mining and Metallurgy. (2019), 119(3): 249–89. Available from: https://dx.doi.org/10.17159/2411-9717/2019/v119n3a7

[32] Pour, A. B., Hashim, M., Hong, J. K., Park, Y. Lithological and alteration mineralmapping in poorly exposed lithologies using Landsat-8 and ASTER satellite data: Northeastern Graham Land, Antarctic Peninsula. (2019), Ore Geology Reviews. v. 108, p. 112-133. https://doi.org/10.1016/j.oregeorev.2017.07.018

[33] Beygi, S., Talovina, I. V., Tadayon, M., Pour, A. B. Alteration and structural features mapping in Kacho-Mesqal zone, Central Iran using ASTER remote sensing data for porphyry copper exploration. (2020), International Journal of Image and Data Fusion, Article in press. https://doi.org/10.1080/19479832.2020.1838628

[34] Bien À Nwos Prisca-Gaëlle, Mounchili Ibrahim, Apouamoun Yiagnigni Roland, Etoundi Jean, Ndongue Constantin and Meying Arsène. The contribution of remote sensing and aeromagnetism to gold prospecting. (2021) the case of the Meiganga zone, Cameroon. http://dx.doi.org/10.21474/ijar01/12903

[35] Gazel, J., Gerard, G. Carte géologique de reconnaissance du Cameroun au 1/500000, feuille de Batouri-Est avec notice explicative. 1954, Mémoire Direction des Mines et de la Géologie, Yaoundé, Cameroun, 43 p.

[36] Milesi JP, Toteu SF, Deschamps Y, Feybesse JL, Lerouge C, Cocherie A, Penaye J, Tchameni R, Moloto-A-Kenguemba G, Kampunzu HAB, Nicol N, Duguey E, Leistel JM, Saint-Martin M, Ralay F, Heinry C, Bouchot V, Doumnang Mbaigane JC, Kanda Kula V, Chene F, Monthel J, Boutin P, Cailteux J. An overview of the geology and major ore deposits of Central Africa: explanatory note for the 1: 4,000,000 map "Geology and major ore deposits of Central Africa. (2006), J Afr Earth Sci 44(4): 571–595. https://doi.org/10.1016/j.jafrearsci (2005.10.016)

[37] Azeuda Ndonfack, K. I., Xie, Y. L., Goldfarb, R. J, Gold occurrences of the Woumbou-Colomine-Kette district, eastern Cameroon: ore-forming constraints from petrography, SEM-CL imagery, fluid inclusions, and C-O-H-S isotopes. (2021a), Miner. Depos. https://doi.org/10.1007/s00126-021-01050-7

[38] Azeuda Ndonfack, K. I., Xie, Y., Goldfarb, R., Zhong, R., Qu, Y. Genesis and mineralization style of gold occurrences of the Lower Lom Belt, Betare Oya district, eastern Cameroon. (2021b), Ore Geology Reviews. https://doi.org/10.1016/j. oregeorev.2021.104586

[39] Ayiwouo1 MN, Mambou1 LLN, Boroh WA, Takougang Ski, Ngounouno I, Spatial variability of trace metals in sediments along the Lom River in the gold mining area of Gankombol (Adamawa Cameroon) using geostatistical modeling methods Modeling. (2022), Earth Systems and Environment https://doi.org/10.1007/s40808-022-01500-9

[40] Toteu SF, Penaye J, Djomani YP. Geodynamic evolution of the Pan-African belt in central Africa with special reference to Cameroon. (2004), J Earth Sci 41(1): 73–85. https://doi.org/10.1139/e03-079.

[41] Penaye J, Toteu SF, Tchameni R, Van Schmus WR, Tchakounté J, Ganwa A, Minyem D, Nsifa EN. The 2.1 Ga West central African belt in Cameroon: extension and evolution. (2004), J Afr Earth Sci 39(3–5): 159–164. http://dx.doi.org/10.1016/j.jafrearsci.2004.07.053

[42] Ganwa AA, Frisch W, Siebel W, Ekodeck GE, Shang CK, Ngako V. Archean inheritances in the pyroxene–amphibole-bearing gneiss of the Méganga area (Central North Cameroon): geochemical and 207Pb/206Pb age imprints. (2008), C R Acad Sci Paris 340(4): 211–222. https://doi.org/10.1016/j.crte.2007.12.009

[43] Ganwa AA, Siebel W, Frisch W, Shang CK, Ekodeck GE. Geochemistry and geochronology of the Méganga metadiorite: implications on the timing of D2 deformational phase in Adamawa Yadé Domain in Cameroon. (2011), Int J Biol Chem Sci 5(4): 1754–1767. https://doi.org/10.4314/ijbcs.v5i4.37

[44] Ganwa AA, Klötzli US, Hauzenberger C Evidence for Archean inheritance in the pre-Panafrican crust of Central Cameroon: insight from zircon internal structure and LA-MC-ICP-MS U-Pb ages. (2016), J Afr Earth Sci 120: 12–22. https://doi.org/10.1016/j.jafrearsci.2016.04.013

[45] Saha Fouotsa AN, Vanderhaeghe O, Barbey P, Eglinger A, Tchameni R, Zeh A, Tchunte PF, Nomo EN. The geologic record of the exhumed root of the Central African Orogenic Belt in the central Cameroon domain (Mbé–Sassa-Mbersi region). (2019), J Afr Earth Sci 151: 286–314. https://doi.org/10.1016/j.jafrearsci.2018.12.008

[46] Soba D, Michard A, Toteu SF, Norman DI, Penaye J. Donnés géochronologiques nouvelles (Rb-Sr, U-Pb et Sm-Nd) sur la zone mobile panafricaine de l'Est du Cameroun: âge protérozoïque supérieur de la série de Lom. (1991), C R Acad Sci Paris 312(12): 1453–1458.

[47] Ngako V, Affaton P, Nnange JM, Njanko T. Pan-African tectonic evolution in central and southern Cameroon: transpression and transtension during sinistral shear movements. (2003), J Afr Earth Sci 36(3): 207–214. https://doi.org/10.1016/S0899-5362(03)00023-X

[48] Toteu SF, Penaye J, Deloule E, Van Schmus WR, Tchameni R. Diachronous evolution of volcano-sedimentary basins north of the Congo craton: insights from U–Pb ion microprobe dating of zircons from the Poli, Lom and Yaoundé Groups (Cameroon). (2006), J Afr Earth Sci 44(4–5): 428–442. https://doi.org/10.1016/j.jafrearsci.2005.11.015

[49] Tchameni R, Pouclet A, Penaye J, Ganwa AA, Toteu SF. Petrography and geochemistry of the Ngaoundéré Pan-African granitoids in Central North Cameroon: implications for their sources and geological setting. (2006), J Afr Earth Sci 44(4): 511–529. https://doi.org/10. 1016/j.jafrearsci.2005.11.017

[50] Njanko, T., Nedelec, A., Affaton, P. Synkinematic high - K calc-alkaline plutons associated to the Pan-African Central Cameroon Shear Zone (W-Tibati area): Petrology and geodynamic significance. (2006), Journal of African Earth Sciences 44, 494-510. https://doi.org/10.1016/j.jafrearsci.2005.11.016

[51] Nzenti JP, Kapajika B, Wörner G, Lubala TR. Synkinematic emplacement of granitoids in a Pan-African shear zone in Central Cameroon. (2006), J Afr Earth Sci 45(1): 74–86. https://doi.org/10.1016/j.jafrearsci.2006.01.005

[52] Kankeu B, Greiling RO. Magnetic fabrics (AMS) and transpression in the Neoproterozoic basement of Eastern Cameroon (Garga-Sarali area). (2006), Neues Jahrbuch für Geologie und Paläontologie - Abhandlungen: 263–287. https://doi.org/10.1127/njgpa/239/2006/263

[53] Kankeu B, Greiling RO, Nzenti JP. Pan-African strike–slip tectonics in eastern Cameroon magnetic fabrics (AMS) and structure in the Lom basin and its gneissic basement. (2009), Precambrian Res 174(3): 258–272. https://doi.org/10.1016/jprecamres.2009.08.001

[54] Asaah, A. V., Zoheir, B., Lehmann, B., Frei, D., Burgess, R., Suh, C. E., Geochemistry and geochronology of the ~620 Ma gold-associated Batouri granitoids. Cameroon. (2015), International Geology Review 57(11–12), 1485–1509. https://doi.org/10.1080/00206814.2014.951003

[55] Nomo Negue E, Takodjou Wambo HD, Yamgouot Ngounouno F, Negou Nembouet J, Teda Soh AC, Tsassé Nganno AS, Fossi DH, Tchameni R. Searching gold origin through litho-structural analysis and morphological characterization of alluvial gold nuggets in the Guiwa-Yangamo area (Batouri goldfield, Eastern Cameroon). (2021), Arab J Geosci 14: 1973. https://doi.org/10.1007/s12517-021-07799-5

[56] Lemdjou YB, Huan Li,. Whattam SA, Azeuda Ndonfack KI,

De pesquidoux I. TT, Ketchaya YB, Quaye JA., Nguimatsia Dongmo FW. Petrogenesis, tectonic setting and geodynamic implications of Ouaden, Doumba Bello, and Ngoura granitic plutons (Eastern Cameroon): Constraints from elemental and Sr−Nd−Hf isotopic data and zircon U−Pb ages. (2022), journal lithos. https://doi.org/10.1016/j.lithos.2022.106682

[57] Nkoumbou C, Barbey P, Yonta-Ngouné C, Paquette J-L, Villiéras F. Pre-collisional geodynamic context of the Southern margin of the Pan-African fold Belt in Cameroon. (2014) J Afri Eath Sci 99(2): 245-260. https://doi.org/10.1016/j.jafrearsci.2013.10.002

[58] Tchakounté J, Eglinger A, Toteu SF, Zeh A, Nkoumbou C, Mvondo Ondoa J, Penaye J, de Wit M, Barbey P The AdamawaYadé domain, a piece of Archaean crust in the Neoproterozoic Central African Orogenic belt (Bafia area, Cameroon). (2017), Precambrian Res 299: 210–229. https://doi.org/10.1016/j.precamres.2017.07.001

[59] Ngako V, Njonfang E, Aka FT, Affaton P, Nnange JM. The North–South Paleozoic to Quaternary trend of alkaline magmatism from Niger–Nigeria to Cameroon: complex interaction between hotspots and Precambrian faults. (2006), J Afr Earth Sci 45(3): 241–256. https://doi.org/10.1016/j.jafrearsci.2006.03.003

[60] Ngounouno F. Y., Nomo E. E., Kolb J., Walter B., Teda A. C. S., Patten C., Ismaïla Ngounouno. Tectonic setting, fluid inclusion and gold mineralization of the southwest Poli region (northern Cameroon Domain). (2022), J Afr Earth Sci 194, 104579. https://doi.org/10.1016/j.jafrearsci.2022.104579

[61] Njonfang E, Nono A, Kamgang P, Ngako V, Tchoua FM. Cameroon Line alkaline magmatism (central Africa): a reappraisal. (2011), Geol Soc Am Spec Pap 478: 173–192. https://doi.org/10.1130/2011.2478(09)

[62] Cornacchia M, Dars R Un trait structural majeur du continent Africain; les lineaments centrafricains du Cameroun au Golfe d'Aden. (1983), Bulletin de la Société Géologique de France S7-XXV (1): 101–109. https://doi.org/10.2113/gssgfbull.S7-XXV.1.101

[63] Almeida FFM, Hasui Y, De Brito Neves BB, Fuck RA. Brazilian Structural Provinces: an introduction. (1981), Earth-Science Review 17: 1-29. http://dx.doi.org/10.1016/0012-8252(81)90003-9

[64] Njonfang E, Ngako V, Moreau C, Affaton P, Diot H. Restraining bends in high temperature shear zones: the "Central Cameroon Shear Zone", Central Africa. (2008), J Afr Earth Sci 52(1): 9–20. https://doi.org/10.1016/j.jafrearsci.2008.03.002

[65] Ngako F, Jegouzo P, Nzenti JP. Le cisaillement centre camerounais. Rôle structural et géodynamique dans l'orogenèse panafricaine. (1991), C Acad sci, Sér 2, Méc phys chim sci univers sci terre 313(4): 457–463.

[66] Soba, D. Le granite de Nyibi et son aureole de contact. (1975), C R Acad Sci Paris 280: 1935.

[67] Lasserre, M. and Soba, D. Âge libérien des granitoïdes et des gneiss à pyroxène du Cameroun méridional. (1976), Bulletin du Bureau de Recherches Géologiques et Minières, 2, 17-32.

[68] Toteu SF, Van Schmus RW, Penaye J, Michard A. New U-Pb and Sm–Nd data from North-Central Cameroon and its bearing on the Pre–Pan–African history of Central Africa. (2001), Precambrian Res 108: 45–73. https://doi.org/10.1016/S0301-9268(00)00149-2

[69] Suh CE, Lehmann B, Mafany GT. Geology and geochemical aspects of lode gold mineralization at Dimako–Mboscorro, SE Cameroon. (2006), Geochemistry: Exploration, Environment, Analysis 6(4): 295–309. https://doi.org/10.1144/1467-7873/06-110

[70] Vishiti, A., Suh, C. E., Lehmann, B., Shemang, E. M., Ngome, N. L. J., Nshanji, N. J., Chinjo, E. F., Mongwe, O. Y., Egbe, A. J., Petersen, S. Mineral chemistry, bulk rock geochemistry, and S‑isotope signature of lode‑gold mineralization in the Bétaré Oya gold district, south‑east Cameroon. (2017), Geological journal, 1-18. http://dx.doi.org/10.1002/gj.3093

[71] Castaing, C., Feybesse, J. L., Thieblemont, D., Triboulet, C., and Chevremont, P. Palaeogeographical reconstructions of the Pan-African/Brasiliano orogen: closure of an oceanic domain or intracontinental convergence between major blocks? (1994), Precambrian Research, 67: 327–344. https://doi.org/10.1016/0301-9268(94)90095-7

[72] Soba D La série de Lom: étude géologique et géochronologique d'un bassin volcanosédimentaire de la chaîne panafricaine à l'Est du Cameroun. (1989), Thèse Doctorat d'Etat, Univ. Pierre et Marie Curie Paris 6, 198p.

[73] Rajendran, S., Nasir, S., Kusky, T. M., Al-Khirbash, S. "Remote sensing based approachfor mapping of CO_2 sequestered regions in Semail ophiolite massifs of the Sultanate of Oman". (2014), Earth Sci. Rev. 135, 122–140. https://doi.org/10.1016/j.earscirev.2014.04.004

[74] Cooley, T., Anderson, G. P., Felde, G. W., Hoke, M. L., Ratkowski, A. J., Chetwynd, J. H., Gardner, J. A., Adler-Golden, S. M., Matthew, M. W., Berk, A., Bernstein, L. S., Acharya, P. K., Miller, D., Lewis P. FLAASH, a MODTRAN4-based atmospheric correction algorithm, its application and validation. (2002), Proceedings of the Geoscience and Remote Sensing Symposium, IEEE International, 3, 1414–1418. http://dx.doi.org/10.1109/IGARSS.2002.1026134

[75] Rajendran, S., Nasir, S., Kusky, T. M., Ghulam, A., Gabr, S., El Ghali, M. "Detection of hydrothermal mineralized zones associated with Listwaenites rocks in the Central Oman using ASTER data". (2013), Ore Geol. Rev. 53, 470–488. https://doi.org/10.1016/j.oregeorev.2013.02.008

[76] Salem, S. M., El Sharkawi, M., El-Alfy, Z., Soliman, N. M., Ahmed, S. E.,. Exploration of gold occurrences in alteration zones at Dungash district, Southeastern Desert of Egypt using ASTER data and geochemical analyses. (2016), J. Afr. Earth Sc. 117, 389–400. https://doi.org/10.1016/j.jafrearsci.2016.01.030

[77] Andongma, W. T.; Gajere, J. N.; Amuda, A. K.; Edmond, R. R. D.; Faisal, M.; Yusuf, Y. D. Mapping of hydrothermal alterations related to gold mineralization within parts of the Malumfashi Schist Belt, North-Western Nigeria. (2021), Egypt. J. Remote Sens. Sp. Sci. 24, 401–417. https://doi.org/10.1016/j.ejrs.2020.11.001

[78] Inzana J., Kusky T., Higgs G., Tucker R. Supervised classifications of Landsat TM band ratio images and Landsat TM band ratio image with radar for geological interpretations of central Madagascar. 2003, Journal of African Earth Sciences – Elsevier. https://doi.org/10.1016/S0899-5362(03)00071-X

[79] Traore, M., Takodjou Wambo, J. D., Ndepete, C. P., Tekin, S., Pour, A. B., Muslim, A. M. Lithological and alteration mineral mapping for alluvial gold exploration in the south east Birao area, Central African Republic using Landsat-8 Operational Land Imager (OLI) data. (2020), Journal of African Earth Sciences 170, 103933. https://doi.org/10.1016/j.jafrearsci.2020.103933

[80] Bonn, F. et Rochon, G. Précis de Télédétection. Principes et méthodes. (1992), Presse de l'université de Québec / AUPELF, vol. 1,485 p.

[81] Cheng, Q., Jing, L., Panahi, A. Principal component analysis with optimum order sample correlation coefficient for image enhancement. (2006), Int. J. Remote Sens. 27(16), 3387–3401. http://dx.doi.org/10.1080/01431160600606882

[82] Gupta, R. P. Remote Sensing Geology, 3rd edn. Springer, Berlin, Germany, pp 180-190, 235-240, and 332-336. https://doi.org/10.1007/978-3-662-55876-8

[83] Shahriari, H.; Ranjbar, H.; Honarmand, M. Image segmentation for hydrothermal alteration mapping using PCA and concentration–area fractal model. (2013), Nat. Resour. Res., 22, 191–206. https://doi.org/10.1007/s11053-013-9211-y

[84] Bell, R. T. & Jefferson, CW. An hypothesis for an Australian-Canadian connection in the Late Proterozoic and the birth of the Pacific Ocean. (1987), Proceedings 'Pacific Rim Congress' 87, 39-50.

[85] Trippa, G. I., Vearncombe, J. R. Fault/fracture density and mineralization: a contouring method for targeting in gold exploration. (2002), Journal of Structural Geology 26(2004), 1087–1108. http://dx.doi.org/10.1016/j.jsg.2003.11.002

[86] Li, N., Frei, M., Altermann, W. Textural and knowledge-based lithological classification of remote sensing data in Southwestern Prieska sub-basin, Transvaal Supergroup, South Africa. (2010), Journal of African Earth Sciences 60 237–246. https://doi.org/10.1016/j.jafrearsci.2011.03.002

[87] Chavez Pat, JR and Brian Bauer. An automatic optimum kernel-size selection technique for edge enhancement. (1982), Remote sensing of environment 12-23-38. https://doi.org/10.1016/0034-4257(82)90005-0

[88] Koffi Yao, T., Fouché-Grobla, O., Yéi Oga, M.-S., Tchimou Assoma, V. Extraction de linéaments structuraux à partir d'images satellitaires et estimation des biais induits en milieu de socle précambrien métamorphisé. (2012), Rev. Teledetect. 10(4), 161–178. https://hal.science/hal-01948904

[89] Scanvic, J.-Y. Utilisation de la télédétection dans les Sciences de la terre. (1983), Manuels et méthodes, 7, B. R. G. M., Orléans, 158 p.

[90] Marion, A. Introduction aux techniques de traitement d'images. (1987), Eyrolles, Paris, pp. 127-167.

[91] Kouamé, K. F., Gioan, P., Biémi, J. et Affian, K. Méthode de cartographie des discontinuités-images satellitales: exemple de la région semi-montagneuse à l'ouest de la Côte d'Ivoire. (1999), Télédétection, vol. 2, pp. 139-156.

[92] Lasm T., Hydrogéologie des réservoirs fracturés de socle: Analyses statistiques et géostatistique de la fracturation et des propriétés hydrauliques. Application à la région des montagnes de Côte d'Ivoire (Domaine Archéen). (2000), Thèse unique de doctorat Université de Poitier, 272p.

[93] Youssouf, K., Alain, N. S., Nakolendousse, S. Les différentes signatures des fractures de socle cristallin en zone sahélo-soudanienne du Burkina Faso (bassin versant de Bidi, province du Yatenga). (2003), Revue de Télédétection 3, 419–427.

[94] Moore, G. K., Waltz, F. A.,. Objective procedure for lineament enhancement and extraction. (1983), Photogrammetric Engineering & Remote Sensing, 49(5): 641–647.

[95] Karnieli A, Meiseis A, Fisher L, Arkin Y. Automatic extraction and evaluation of geological linear features from digital remote sensing data using a Hough Transform. (1996), Photogramm Eng Remote Sens 62:525–531.

[96] Wladis, D., Automatic lineament detection using digital elevation models with second derivative filters. (1999), Photogrammetric Engineering and Remote Sensing 65(4), 453–458.

[97] Youan Ta M. Contribution de la télédétection des systèmes d'informations géographiques à la prospection hydrogéologique du socle Précambrien d'Afrique de l'Ouest: cas de la Région de Bondokou (Nord-est de la Cote Ivoire). (2008), Thèse de Doctorat à l'université de Cocody, 273pages.

[98] Caldini F. G., Posavec M., Azuelos M. J. Carte photogéologique de la Côte d'Ivoire à 1/200 000, Feuille de Nassian, Commission du Canada. (1978), Société pour de Développement Minier de la Côte d'Ivoire (SODEMI).

[99] Delor C., Simeon Y., Vidal M., Zeade Z., Kone Y., Adou M., Dibouahi J., Irie D. B., Ya B. D., N'da D., Pouclet A., Konan G., Diaby I., Chiron J-C., Dommanget A., Kouamelan A., Peucat J. J., Cocherie A. Et Cautru J. P. (1995), Carte géologique de la Côte d'Ivoire à 1/200 000, feuille Nassian, Mémoire n°9 de la Direction des Mine et de la Géologie, Abidjan.

[100] Zeade, Z., Delor, C., Simeon, Y., Yao, B. D., Vidal M, Sonnendrucker, P., Diaby, I., Cautru, J. p. (1995), Notice explicative de la carte Géologique de la Côte d'Ivoire à 1/200 000, Feuille Bondoukou, Mémoire de la Direction des Mines et de la Géologie de la Côte d'Ivoire, n°10 Abidjan, Côte d'Ivoire.

[101] Khosroshahizadeh, S., Pourkermani, M., Almasiyan, M., Arian, M., Khakzad, A., Evaluation of Structural Patterns and Related Alteration and Mineralization Zones by Using ASTER Imagery in Siyahrood Area (East Azarbaijan-NW Iran). (2015), Journal of Geosciences and Geomatics 95. Open Journal of Geology, 5, 589-610.

http://dx.doi.org/10.4236/ojg.2015.59053

[102] Faillat, J.-P. Aquifères fissurés en zone tropicale humide: structure, hydrodynamique et hydrochimie. (1986), Thèse de Doctorat 'État, Université du Languedoc-Monptpellier II, 536 p.

[103] Lasm, T. et Razack, M. Lois d'échelle dans la fracturation de roches dures cristallines et dans le réseau hydrographique. (2001), Compte Rendu de l'Académie des Sciences, Series IIA - Earth and Planetary Science, vol. 333, n°4, pp. 225-232. http://dx.doi.org/10.1016/S1251-8050(01)01632-9

[104] Lasm T., Razack M., Youan Ta M. Geostatistical assessment of the transmissivity of crystalline fissured aquifer in the Bondoukou region, north-eastern Côte d'Ivoire. (2004), Applied groundwater Studies in Africa; n° 13, chapiter 28, 473-485.

[105] Kouamé K. F., Akaffou A. G., Lasm T., De Dreuzy J. R., Davy P. & Bour O. Simulation des écoulements dans les réservoirs fracturés: application au socle Archéen de Touba (Nord-Ouest de la Côte d'Ivoire). (2005), Actes du Colloque Internationale SITIS 05, Yaoundé (Cameroun), 27 Nov.-1er Déc. pp. 39-46.

[106] Cheval-Garabédian F, Faure M, Marcoux E, Poujol M. The tungsten-gold veins of Bonnac (French Massif Central): new constraints for a Variscan granite-related genesis. (2021), BSGF - Earth Sciences Bulletin 192: 7. http://dx.doi.org/10.1051/bsgf/2020041

[107] Poitrenaud T, Marcoux É, Augier R, Poujol M. The perigranitic W-Au Salau deposit (Pyrenees, France): polyphaser genesis of a late Variscan intrusion related deposit. (2021), BSGF - Earth Sciences Bulletin 192: 22. https://doi.org/10.1051/bsgf/202004

[108] Loughlin W. Principal component analysis for alteration mapping. (1991), Photogrammetric Engineering and Remote Sensing, 57, 1163–1169.

[109] Zhang, X., Pazner, M., Duke, N. Lithologic and mineral information extraction for gold exploration using ASTER data in the south chocolate mountains (California). (2007), ISPRS Journal of Photogrammetry & Remote Sensing, 62, 271–282. https://doi.org/10.1080/01431160903124682

[110] Liu X, Xing H, Zhang D. Influences of hydraulic fracturing on fluid flow and mineralization at the vein-type tungsten deposits in southern China. (2017), Geofluids: 1–11. https://doi.org/10.1155/2017/4673421

[111] Hammam, A., Gaber, A., Abdelwahed, M., Hammed, M. Geological mapping of the Central Cairo-Suez District of Egypt, using space-borne optical and radar dataset. (2018), the Egyptian Journal of Remote Sensing and Space Sciences 23(3), 275-285. https://doi.org/10.1016/j.ejrs.2018.11.004

[112] Kumar, C., Chatterjee, S., Oommena, T., Guha. A. Automated lithological mapping by integrating spectral enhancement techniques and machine learning algorithms using AVIRIS-NG hyperspectral data in Gold-bearing granite-greenstone rocks in Hutti, India. (2020), Int J Appl Earth Obs Geoinformation 86, 102006. https://doi.org/10.1016/j.jag.2019.102006

[113] Adiri, Z., Lhissou, R., El Harti, A., Jellouli, A., Chakouri, MRecent advances in the use of public domain satellite imagery for mineral exploration: A review of Landsat-8 and Sentinel-2 applications. (2020), Ore Geology Reviews 117. https://doi.org/10.1016/j.oregeorev.2020.103332

[114] Pour, A. B., Sekandari, M., Rahmani, O., Crispini, L., Läufer, A., Park, Y., Hong, J. K., Pradhan, B., Hashim, M., Hossain, M. S., Muslim, A. M., Mehranzamir, K., Identification of Phyllosilicates in the Antarctic Environment Using ASTER Satellite Data: Case Study from the Mesa Range, Campbell and Priestley Glaciers, Northern Victoria Land. (2021), Remote Sens. 2021, 13, 38. https://doi.org/10.3390/rs13010038

[115] Harlaux M, Romer RL, Mercadier J, Morlot C, Marignac C, Cuney M. 40 Ma of hydrothermal W mineralization during the Variscan orogenic evolution of the French Massif Central revealed by U-Pb dating of wolframite. (2018), Miner Depos 53: 21–51. https://doi.org/10.1007/s00126%E2%80%93017%E2%80%93072 1-0

[116] Gabr S, Ghulam A, Kusky T. Detecting areas of high-potential gold mineralization using ASTER data. (2010), Ore Geol Rev 38:59–69. https://doi.org/10.1016/j.oregeorev.2010.05.007

[117] Ruiz-Armenta, J. R., & Prol-Ledesma, R. M. Techniques for enhancing the spectral response of hydrothermal alteration minerals in the Thematic Mapper images of Central Mexico. (1998), International Journal of Remote Sensing, 19(10), 1981–2000. https://doi.org/10.1080/014311698215108

[118] Han, T. & Nelson, J. Mapping hydrothermally altered rocks with Landsat 8 imagery: Acase study in the KSM and Snow field zones, northwestern British Columbia. (2015), In: Geological Fieldwork 2014, British Columbia Ministry of Energy and Mines, British.

[119] Ngassam GM, Timoleon N, Takodjou Wambo J D, Ganno S, Beiranvand AP, Ayonta PK, Fossi DH, Isabelle D. Wolf. Remote sensing satellite-based structural/alteration mapping for gold exploration in the Kettégoldfield, Eastern Cameroon. (2021), journal of African Earth Sciences https://doi.org/10.1016/j.jafrearsci.2021.104386

[120] Dumont, J. F., Toteu, S. F., et Penaye, J. Ensembles structuraux et principales phases de déformations panafricaines dans la zone mobile du Nord Cameroun, région de Poli. (1985), Revue des Sciences et Techniques, Série Sciences de la Terre, Yaoundé, 1: 9–23.

[121] Neves, SP., Melo, SC., Moura, CAV., Mariano, G., Silva, JMR. Zircon Pb-Pb geochronology of the Caruaru area, north-eastern Brazil: temporal constraints on the Proterozoic evolution of Borborema Province. (2004), International Geology Review, 46, 52-63. https://doi.org/10.2747/0020-6814.46.1.52

[122] Kankeu, B., Greiling, R. O., Nzenti, J. P., Bassahak, J., Hell, V. J.,. Strain partitioning along the neoproterozoic central Africa shear zone system: magnetic fabrics (AMS) and structures from the Meiganga area, Cameroon. (2012), Neues Jahrb. für

Geol. Palaontologie Abh. 265, 27-48. http://dx.doi.org/10.1127/0077-7749/2012/0244

[123] Vishiti, A., Suh, C. E., Etame, J. Features of gold-bearing quartz veins in an artisanal mining dominated terrain, Batouri gold district, Eastern region of Cameroon. (2019), IUGS, Episodes Vol. 42, No. 3, 199-212. http://dx.doi.org/10.18814/epiiugs/2019/019016

[124] Al-Mokredi, M. S., Guangdao, H., Al Bassam, B. F. Using Remote Sensing Data to Delineate the Lineaments for Hydrothermal Mineral Prediction in Heqing Area, Northwest Yunnan Province, China. (2007), Journal of China University of Geosciences, vol. 18, No. 2, p. 142-147. http://dx.doi.org/10.1016/S1002-0705(07)60028-4

[125] Takodjou Wambo, J. D., Ganno, S., Afahnwie, N. A., Nomo, N. E., Mvondo, O. J., Nzenti, J. P. Use of Landsat 7 ETM+ data for the geological structure interpretation: case study of the Ngoura Colomines area, Eastern Cameroon. (2016), Journal of Geoscience and Geomatics 4(3), 61–72. http://dx.doi.org/10.12691/jgg-4-3-3

[126] Nguemhe Fils, S. C., Bekele Mongo, C. H., Nkouathio, D. G., Mimba, M. E., Etouna, J, Njandjock Nouck, P., Brunot Nyeck, B. Radarsat-1 image processing for regionalscale geological mapping with mining vocation under dense vegetation and equatorial climate environment, Southwestern Cameroon. (2018), The Egyptian Journal of Remote Sensing and Space Sciences 21, S43–S54. https://doi.org/10.1016/j.ejrs.2018.05.005

[127] Groves DI. The crustal continuum model for late-Archaean lodegold deposits of the Yilgarn Block, Western Australia. (1993), Mineral Deposita 28(6): 366–374. https://doi.org/10.1007/BF02431596

[128] Chauvet A, Piantone P, Barbanson L, Nehlig P, Pedroletti I Gold deposit formation during collapse tectonics: structural, mineralogical, geochronological, and fluid inclusion constraints in the Ouro Preto gold mines, Quadrilátero Ferrífero, Brazil. (2001), Econ Geol 96(1): 25–48. https://doi.org/10.2113/gsecongeo.96.1.25

[129] Saint-Jean, R. The role of the eco in the context of the international charter on space and major disasters. (2005), IEEE International Geoscience and Remote Sensing Symposium (IGARSS), Seoul, Korea (South), 25-29 July, 6, 4370-4372.

[130] Van Krieken AT. and Wilson CJL. Structural and timing constraints on molybdenum and tungsten mineralization at Yea, Victoria. (2016), Australian Journal of Earth Sciences. https://doi.org/10.1080/08120099.2015.1121927

[131] De Roo J. A. Structural controls on the emplacement of the vein-type tungsten-tin ore at Mount Carbine, Queensland, Australia. (1988), Economic Geology 83(6): 1170–1180. https://doi.org/10.2113/gsecongeo.83.6.1170

[132] Mayachar GK. and Ghosh S. Fluid Inclusion Characteristics of Tungsten Mineralization in the Agargaon Area of Sakoli Fold Belt, Central India. (2020), Mineral Deposits. http://dx.doi.org/10.1007/s12583-019-1271-4